



CrossMark
click for updates

Cite this: *Lab Chip*, 2015, 15, 4166

A spatiotemporally controllable chemical gradient generator *via* acoustically oscillating sharp-edge structures†

Po-Hsun Huang,^a Chung Yu Chan,^a Peng Li,^a Nitesh Nama,^a Yuliang Xie,^{ab} Cheng-Hsin Wei,^c Yuchao Chen,^a Daniel Ahmed^a and Tony Jun Huang^{*ab}

The ability to generate stable, spatiotemporally controllable concentration gradients is critical for resolving the dynamics of cellular response to a chemical microenvironment. Here we demonstrate an acoustofluidic gradient generator based on acoustically oscillating sharp-edge structures, which facilitates in a step-wise fashion the rapid mixing of fluids to generate tunable, dynamic chemical gradients. By controlling the driving voltage of a piezoelectric transducer, we demonstrated that the chemical gradient profiles can be conveniently altered (spatially controllable). By adjusting the actuation time of the piezoelectric transducer, moreover, we generated pulsatile chemical gradients (temporally controllable). With these two characteristics combined, we have developed a spatiotemporally controllable gradient generator. The applicability and biocompatibility of our acoustofluidic gradient generator are validated by demonstrating the migration of human dermal microvascular endothelial cells (HMVEC-d) in response to a generated vascular endothelial growth factor (VEGF) gradient, and by preserving the viability of HMVEC-d cells after long-term exposure to an acoustic field. Our device features advantages such as simple fabrication and operation, compact and biocompatible device, and generation of spatiotemporally tunable gradients.

Received 24th July 2015,
Accepted 26th August 2015

DOI: 10.1039/c5lc00868a

www.rsc.org/loc

Introduction

The spatial and temporal dynamics of biomolecule gradients are essential in many biological processes.^{1–6} It has been reported that cells respond differently to spatial and temporal characteristics of chemical stimuli, which in turn influences cell signalling,^{7–9} migration,^{10–15} differentiation,^{16–18} and metastasis.^{19,20} Conventional gradient-generation platforms such as the Boyden chamber and derivatives^{21–23} as well as micropipette^{24,25} have been adopted because of their simplicity of fabrication and ease of use. These platforms, however, are limited to generating only static, monotonic gradients without tunable spatiotemporal characteristics (*e.g.*, magnitude, frequency, slope, and temporal and spatial resolution).

To explore the effect of the time and space dynamics of gradients on cellular responses, microfluidic platforms have been advanced to generate chemical gradients with spatiotemporal control, including Christmas-tree-like channel networks,^{26,27} microjet arrays,^{28,29} and source-sink configuration.^{30–32} Most of these microfluidic-based gradient generators still employ passive means, either passive mixing^{33,34} or free-diffusion,^{35–38} making these approaches difficult to generate gradients with high spatiotemporal resolution. In contrast to passive generation of concentration gradients, actively generating concentration gradients offers compelling controllability and flexibility. One can envision a microfluidic-based device that can—by active and controllable means, “active mixing”—generate concentration gradients of biomolecules of interest with highly controllable specific spatiotemporal characteristics.

Recently, active generation of gradients has been demonstrated using acoustofluidic-based platforms; two of the most intriguing platforms are focused travelling surface acoustic waves (F-TSAW)³⁹ and acoustically oscillating microbubbles.⁴⁰ Though the F-TSAW based platform generated gradients that can be rapidly switched on and off and the resulting gradient profiles can be easily adjusted, it is limited to generating only monotonic (mono-directional) gradients, and its applicability and biocompatibility are yet unproven for biological studies. The oscillating microbubbles-based platform, likewise, can

^a Department of Engineering Science and Mechanics, The Pennsylvania State University, University Park, PA 16802, USA. E-mail: junhuang@psu.edu

^b Department of Chemical Engineering, The Pennsylvania State University, University Park, PA 16802, USA

^c Department of Nutritional Sciences, The Pennsylvania State University, University Park, PA 16802, USA

† Electronic supplementary information (ESI) available: Video S1 – acoustic streaming patterns generated in our device. Video S2 – generation of chemical gradient at sharp-edge region. Video S3 – generation of chemical gradient at downstream regions. Video S4 – generation of different types of chemical gradient. Video S5 – spatiotemporally controlled generation of chemical gradients. Video S6 – the movement of HMVEC-d cells in response to a VEGF gradient. See DOI: 10.1039/c5lc00868a

generate spatiotemporally tunable gradients. However, the instability of microbubbles over time^{41–44} and the size-/temperature-dependent operation of the platform make it unsuitable for biological applications where long-term cell culture is often needed, thereby limiting the versatility of this approach.

Here we demonstrate an active, spatiotemporally controllable chemical gradient generator *via* an acoustofluidic^{45–60} (*i.e.*, the fusion of acoustics and microfluidics) strategy. This work is built primarily upon our previously reported oscillating sharp edges induced acoustic streaming effects.^{61–64} We have shown that the sidewall sharp-edge-based mixer⁶¹ is capable of rapidly mixing fluids in microscale on-demand. In spite of these features, the sidewall sharp-edge-based mixer we demonstrated previously⁶¹ can only yield constant concentrations. In order to achieve the concentration gradients, in this work we employed multiple sharp-edge structures to form multiple mixing sites at once. In addition, instead of attaching the sharp edges to the sidewall of the channel, as we demonstrated previously,^{61–64} we arranged the sharp-edge structures in the middle of the channel in a ladder-like arrangement.

By taking advantage of these newly designed device features, we can mix two different solutions in a step-wise fashion and thus, obtain different mixtures of serially diluted concentrations simultaneously in the channel; in other words, we can serially dilute the mixture of two different solutions to establish a concentration gradient. Furthermore, once various flow rate combinations of two solutions are introduced to the device, we can, accordingly, mix two solutions in various ratios, resulting in various gradient profiles. Using this sharp-edge-based acoustofluidic gradient generator, one can generate a concentration gradient that is not only spatiotemporally stable, but also spatiotemporally controllable. Spatiotemporal control over gradient profiles can be easily achieved by adjusting the input signal of a piezoelectric transducer (frequency, voltages, and actuation time). Compared to existing microfluidic-based gradient generators,^{39,40} our acoustofluidic gradient generator features distinct characteristics such as stability, controllability, flexibility, reliability, simplicity, and temporal response. Our platform is a promising candidate for a wide variety of biological studies where the spatiotemporal dynamics of gradients is highly relevant.

Concept and device design

Fig. 1a illustrates the design and concept of our acoustofluidic device for the generation of chemical gradients. The device is simple: a single-layer polydimethylsiloxane (PDMS) channel accommodating multiple sharp-edge structures inside the channel and a piezoelectric transducer. Fluids of different compositions or concentrations—for this example, phosphate buffered saline (PBS) and PBS containing fluorescein isothiocyanate-dextran (FITC-dextran)—are simultaneously injected into the channel through two separate

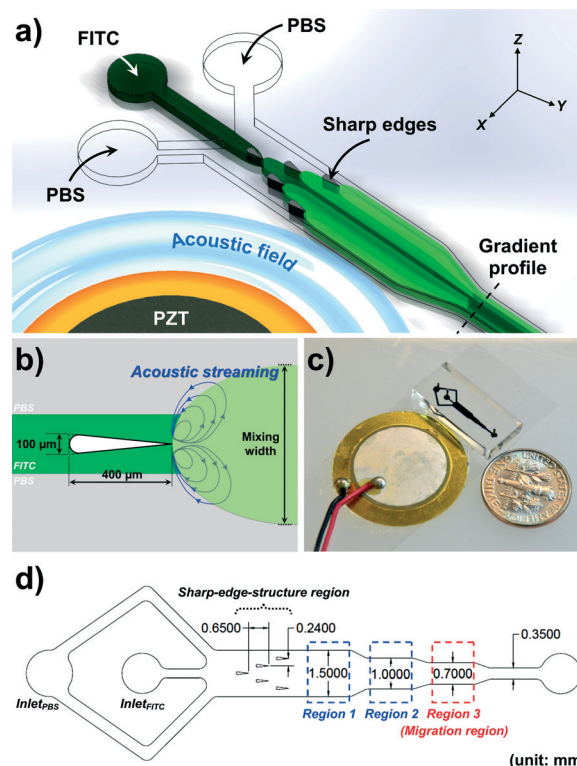


Fig. 1 (a) Schematic of the acoustofluidic chemical gradient generator. (b) Schematic of the sharp-edge structure within our device. (c) Optical image of the acoustofluidic chemical gradient generator. (d) Design of the acoustofluidic gradient generator. To demonstrate controllable spatial resolution of generated chemical gradients, the downstream region of the device is divided into three regions: region 1, region 2, and region 3.

inlets. Before the piezoelectric transducer was activated, a side-by-side laminar flow of PBS and FITC-dextran was observed. Once the piezoelectric transducer was activated, the sharp-edge structures acoustically oscillated and thereby generated acoustic streaming effects around the tip of each sharp-edge structure (Fig. 1b). The induced acoustic streaming effects in turn mixed PBS and FITC-dextran in a step-wise fashion because of the ladder-like arrangement of sharp-edge structures. The step-wise mixing established a concentration gradient of FITC-dextran which was perpendicular to the direction of fluid flow, *i.e.*, along the direction of channel width (dotted line in Fig. 1a).

Fig. 1b illustrates an acoustic streaming pattern around the tip of a sharp-edge structure, as well as the mixing of different solutions due to the generated acoustic streaming effect. Each sharp-edge structure constructed inside the channel was of identical dimension to ensure that all sharp-edge structures would be acoustically excited at a single driving frequency from the piezoelectric transducer; in other words, it was to ensure that the acoustic streaming effect induced by each oscillating sharp-edge structure was identical in terms of strength. In order to eliminate undesired acoustic streaming effects, the sharp-edge structure was designed to be tear-drop-like, based upon a triangular structure of width 100 μm

and length 400 μm . Once it was acoustically oscillated by the actuation of the piezoelectric transducer, the oscillating sharp-edge structure generated an acoustic streaming effect around its tip: mass transport across the channel width was enhanced (*i.e.*, different fluids were mixed by breaking the interface of laminar fluids). The mixing width was defined as the width over which the generated acoustic streaming effect spanned across the channel; in other words, the mixing width can be an index of the strength of generated acoustic streaming effect. A lesser “mixing width” allowed the FITC-dextran to mix with a small amount of PBS, gently diluting the FITC-dextran. A greater mixing width, by contrast, allowed the FITC-dextran to mix with a significant amount of PBS, greatly diluting the FITC-dextran. Given that the mixing width was proportional to the strength of the acoustic streaming effect and the strength was controllable by varying the driving voltage of the piezoelectric transducer, we adjusted the mixing width by controlling the driving voltage. We were able to alter the concentration of the resulting mixture by changing the driving voltage of the piezoelectric transducer.

Materials and methods

Experimental setup and operation

Fig. 1c is a photograph showing our acoustofluidic device for generating concentration gradients. The preparation of our device is simple and of one-layer fabrication. In short, a single-layer PDMS device was first prepared using soft lithography and the mold-replica technique. Afterward, the single-layer PDMS channel was bonded onto a glass slide of 150 μm thickness (Cat. no. 48404-454, VWR, USA) after a plasma surface-treatment for 60 seconds (BD-10AS, Electro-Technic Products, IL, USA), followed by bonding a piezoelectric transducer (Model no. 273-073, RadioShack, USA) adjacent to the PDMS device on the same glass slide with a thin layer of epoxy (Part no. 84101, Permatex, CT, USA). The actuation of the piezoelectric transducer, including ON/OFF switching, driving frequency and voltage, and actuation time, was controlled by a function generator (AFG3011C, Tektronix, USA) and an amplifier (25A250A, Amplifier Research, USA).

Fig. 1d shows the detailed channel design of our device. The channel depth was 100 μm throughout the channel. To show the spatial distribution of concentration gradient, the channel downstream from the sharp-edge-structure region was designed to accommodate multiple regions of various channel widths: region 1 (1500 μm), region 2 (1000 μm), and region 3 (700 μm). Region 3, here called the “migration region”, was particularly designed to be 700 μm wide for the demonstration of cell migration experiment with our device. The width of the channel defines the width of the gradient profiles generated. The sharp-edge structures were 650 μm and 240 μm apart, respectively, along the direction of channel width (*x*-direction) and length (*y*-direction). The arrangement of sharp-edge structures, as shown in Fig. 1d, is optimized primarily based on the mixing width (*i.e.*, the width of

one paired streaming-pattern) that one sharp-edge structure can generate when acoustically oscillated. Nevertheless, it is worth mentioning that by changing the arrangement of sharp-edge structures, the concentration gradient profiles might be altered accordingly.

As our acoustofluidic gradient generator works by driving the piezoelectric transducer, the working frequency of the transducer was experimentally determined by sweeping frequency with a 50 Hz increment from 1 kHz to 100 kHz. We observed that when the piezoelectric transducer was activated at 14.0 kHz, the sharp-edge structures generated strongest acoustic streaming effect. When operated at this frequency, our device maximized the mixing distance as shown in Fig. 1c, indicating that more solutions could be mixed when other experimental conditions such as input voltages and flow rates remained unchanged. The frequency of 14.0 kHz was thus used in following experiments.

To characterize the generated concentration gradients, phosphate buffered saline (1 \times -PBS, Life Technology, CA, USA) and PBS containing FITC-dextran (1 mg mL⁻¹; MW = 10 kDa, Sigma-Aldrich, MO, USA) were pumped into the channel through two distinct inlets. The injection of these two solutions was performed using two separate 1 mL syringes (BD Bioscience, NJ, USA), which were independently controlled by an automated syringe pump (neMESYS, Germany).

All of the experiments were conducted on the stage of an inverted microscope (TE2000-U, Nikon, Japan) that was equipped with a cell incubation system (Chamlide TC, Live Cell Instrument, South Korea). The cell incubation system provides a humidified environment at 37 °C with a CO₂ level of 5% for on-chip cell culture. All the experimental images and videos were captured using Nikon NIS-Elements Advanced Research (AR) software, and the image and video processing were conducted using ImageJ (NIH, MD, USA).

Cell preparation

Human dermal microvascular endothelial cells (HMVEC-d, ATCC, VA, USA) were grown in EndoGRO-LS complete media (Millipore, MA, USA) in a CO₂ incubator (Nu-4750, NuAire, MN, USA), which maintained a temperature of 37 °C and a CO₂ level of 5%. Cells grown to 80–90% confluency were trypsinized (Trypsin-EDTA-0.05%, Gibco, Life Technologies, NY, USA), washed with PBS, re-suspended in a new culture medium at desired cell concentrations, and seeded into the channel for experimentation.

Cell migration

In order to verify if the concentration gradients generated by our acoustofluidic gradient generator can be applicable for cell studies, cell migration experiments using HMVEC-d cells were conducted with our gradient generator. To do so, HMVEC-d cells were cultured on-chip inside the channel of our device. The channels were first coated with fibronectin (100 $\mu\text{g mL}^{-1}$; Cat. no. 356008, BD Biosciences, NJ, USA) for 1 hour. After coating, the channels were flushed with PBS

several times to remove residual fibronectin. Suspended HMVEC-d cells (1×10^6 cells mL^{-1}) were then injected into the channel through the PBS inlet (Inlet_{PBS}), and as such they were dispersed mostly near both sidewalls of the channel. The cells were allowed for 30 minutes to adhere to the bottom surface of the device coated with fibronectin. Once they adhered to the substrate, pure EndoGro-LS media and EndoGro-LS media mixed with Human VEGF 165 (50 ng mL^{-1} ; Cat. no. 293-VE-010, R&D systems, MN, USA; here called "VEGF") were injected into the channel, respectively, through the PBS inlet and the FITC inlet (Inlet_{FITC}) at a flow rate ratio of 5 ($R_{\text{FLOW}} = 5$; $Q_{\text{EndoGro}} = 2.5 \text{ mL min}^{-1}$ to $Q_{\text{VEGF}} = 0.5 \text{ mL min}^{-1}$). Prior to the onset of establishing a VEGF gradient, we took an image to record the initial positions of the HMVEC-d cells ($t = 0$ hours). Once the VEGF gradient was established, images were taken every 5 minutes to record cell movement. After 6 hours, the VEGF gradient was shut off, and the cell migration region was divided into three zones (two side zones and one center zone). We tracked the movement of those cells seeded initially in two side zones, while those seeded in the center zone were excluded because they barely moved in response to a high-concentration VEGF after 6 hours (Fig. S1†).

We determined the number of cells for different types of movement. For comparison, cell migration experiments in which cells were exposed to only EndoGro medium were conducted as a negative control (N-control). In addition, as a positive control (P-control), cell migration experiments were conducted with media of the same conditions as the experimental group, but the VEGF gradient was OFF-state (in the absence of acoustic field). Three independent experiments were carried out for each of the three groups.

Cell viability

To evaluate the biocompatibility of our acoustofluidic gradient generator for cell study, cell viability in our device was assessed after lasting exposure to an acoustic field. The assessment of cell viability was carried out by staining the HMVEC-d cells with live-stain Calcein-AM (CaAM) (Life Technologies, NY, USA) and propidium iodide (PI) (Sigma-Aldrich, MO, USA) after exposure to the acoustic field for 6 hours in our device. To do so, 1 mL PBS containing 1 μL Calcein-AM as well as 1 μL PI was infused into the channel at a flow rate of 2 $\mu\text{L min}^{-1}$ for 15 minutes. Afterward, pure PBS was injected at a flow rate of 2 $\mu\text{L min}^{-1}$ for 15 minutes to wash out residual viability dyes. As a control group, we assessed the cell viability of those HMVEC-d cells which were cultured in the channel for 6 hours with no exposure to the acoustic field. Three independent experiments were performed for both the control and experimental groups.

Statistical analysis

Data were presented as group means \pm standard deviation (SD), and were analyzed by one-way ANOVA test using Prism

6.0 (GraphPad Software Inc., CA, USA). Differences among treatment groups were determined by Tukey's Multiple Comparison test. A p -value of less than 0.05 was considered statistically significant.

Results and discussion

Characterization of flow patterns in our device

The shape and arrangement of the sharp-edge structures were redesigned in this work, differing greatly from structures designed in our previous work.^{61–64} We first conducted experiments to verify if the sharp-edge structures, once acoustically oscillated by the piezoelectric transducer, can induce acoustic streaming effects in the channel. Therefore, we first visualized and characterized the flow patterns and the acoustic streaming patterns generated inside the channel of our acoustofluidic device, by injecting into the channel DI water containing dragon green fluorescent beads of 1.9 μm diameter (Bangs Laboratories, IN, USA). Fig. 2 shows the experimentally observed and numerically simulated flow patterns and acoustic streaming effects at the sharp-edge-structure region. Without a background flow, the fluorescent beads remained stationary in the absence of an acoustic field (*i.e.*, the piezoelectric transducer was inactivated), as shown in Fig. 2a. In the presence of an acoustic field (*i.e.*, the piezoelectric transducer was activated), acoustic streaming effects developed around the tip of each sharp-edge structure as a result of acoustically oscillating sharp-edge structures, as shown in Fig. 2b. Upon the introduction of a background flow (from left to right), a laminar flow profile was observed when the piezoelectric transducer was inactivated (Fig. 2d); once the piezoelectric transducer was activated, the acoustic streaming effect could develop around the tip of each sharp-edge structure. It is worth noting that the background flow significantly suppressed the acoustic streaming pattern to narrow rolls, as shown in Fig. 2e. A real-time video showing the flow profiles and the acoustic streaming patterns developed inside the channel can be found in ES1† (Video S1).

To understand the complex flow patterns developed inside the microfluidic channel with sharp-edge structures, we conducted numerical simulations of the bead trajectories. The acoustic streaming flow was calculated using the perturbation approach.⁶⁵ The details of this approach and the particle tracking methodology can be found elsewhere.⁶² The numerical simulations of particle trajectories both without and with the background flow are shown in Fig. 2c and f, respectively. The numerical results are in good qualitative agreement with the experimentally observed trajectories. It was observed in simulations that the background flow velocity can be tuned in conjunction with the input power of acoustic actuation to control the suppression of the acoustic streaming. The correspondence between flow patterns both experimentally observed and numerically simulated implies that the operation of our device can be predicted and controlled.

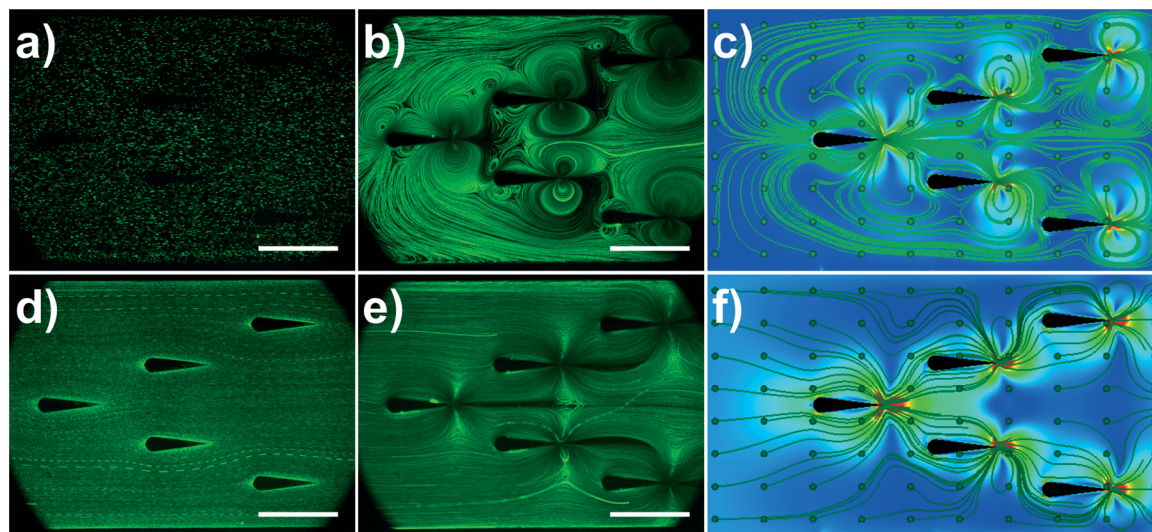


Fig. 2 (a) Fluorescent polystyrene beads seeded randomly inside the microchannel for visualization of flow profiles. (b) Experimentally observed streaming profile around the sharp-edge structures on acoustic actuation visualized via trajectories of 1.9 μm diameter fluorescent beads. (c) Numerically simulated trajectories of 80 beads seeded uniformly inside the channel showing good qualitative agreement with the experimental results in (b). (d) Flow profile around sharp-edge structures due to a background laminar flow in the absence of acoustic actuation. (e) Experimentally observed trajectories of 1.9 μm diameter fluorescent beads. These resulted from the combination of acoustically generated streaming and the background laminar flow. (f) Numerically simulated trajectories of 80 beads seeded uniformly inside the channel about the structures shown in (e). Scale bar: 500 μm .

Generation of concentration gradients

In this section, we validated the generation of concentration gradient using PBS and FITC-dextran solutions. The two solutions were independently pumped into the channel at different flow rates ($Q_{\text{PBS}} = 2.5 \mu\text{L min}^{-1}$ & $Q_{\text{FITC}} = 0.5 \mu\text{L min}^{-1}$). Unless otherwise specified, in this work the flow rate ratio ($R_{\text{FLOW}} = Q_{\text{PBS}}/Q_{\text{FITC}} = 5$) of PBS and FITC-dextran remained constant for all experiments. To quantitatively characterize the concentration gradients generated using our device, fluorescent images were captured from different regions: sharp-edge-structure region, region 1, region 2, and the migration region (region 3), followed by normalizing their fluorescence intensity to that of 100% FITC-dextran (1 mg mL^{-1}) measured at the region upstream the sharp-edge-structure region. Fig. 3a–c show the fluorescent images of FITC-dextran concentration gradients at different regions and under different input voltages. When the piezoelectric transducer was off, a side-by-side laminar flow was observed due to low Reynolds number in the microfluidic channel (Fig. 3a). Once the piezoelectric transducer was turned on with a voltage of 10 V_{PP} , the acoustic streaming induced mixing in a step-wise fashion, thereby generating concentration gradients of FITC-dextran (Fig. 3b). As the input voltage was increased to 15 V_{PP} , the mixing width increased owing to the increase in the strength of acoustic streaming; as a result, FITC-dextran (bright portion) was mixed with more PBS (dark portion), generating a shallower FITC-dextran gradient than that generated by 10 V_{PP} .

Fig. 3d–f show the corresponding normalized gradient profiles under different input voltages at the three regions

(with different channel widths) downstream the channel. When the piezoelectric transducer was OFF, steeper gradient profiles were formed solely from the free diffusion of PBS and FITC-dextran. As the input voltage was increased, the increased mixing width enabled the mixing of FITC-dextran with more PBS buffer, forming shallower gradient profiles. Once a driving voltage of 25 V_{PP} was applied, a nearly flat gradient profile was established because the mixing spanned the entire channel due to stronger acoustic streaming. The results demonstrate that by adjusting the input voltage (*i.e.*, adjusting the mixing distance), the gradient profiles are modulated, proving our acoustofluidic gradient generator spatially controllable. Additionally, the plots also illustrate that the width of gradient profiles could be tuned over a range, in this work from 1500 μm to 700 μm , by changing the width of the channel downstream. We expect that the width of gradient profile can be further widened to several millimeters, or narrowed down to 50 μm .³⁴ By alternating the piezoelectric transducer, the gradient could be actively formed and removed in real time (Video S2[†]), and even in downstream regions the gradient could still be established and shut off within just a few seconds (Video S3[†]). This not only shows the temporal controllability of our device, but also reveals that we can expose cells from one gradient to another (*e.g.*, from gradient-OFF to gradient-ON) within a few seconds.

To demonstrate the flexibility of our sharp-edge-based gradient generator, furthermore, we constructed the sharp-edge structures in an arrangement which established another gradient profile. As shown in Fig. S2[†] we reconfigured the arrangements of the sharp-edge structures to establish another type of gradient profile. With this specific

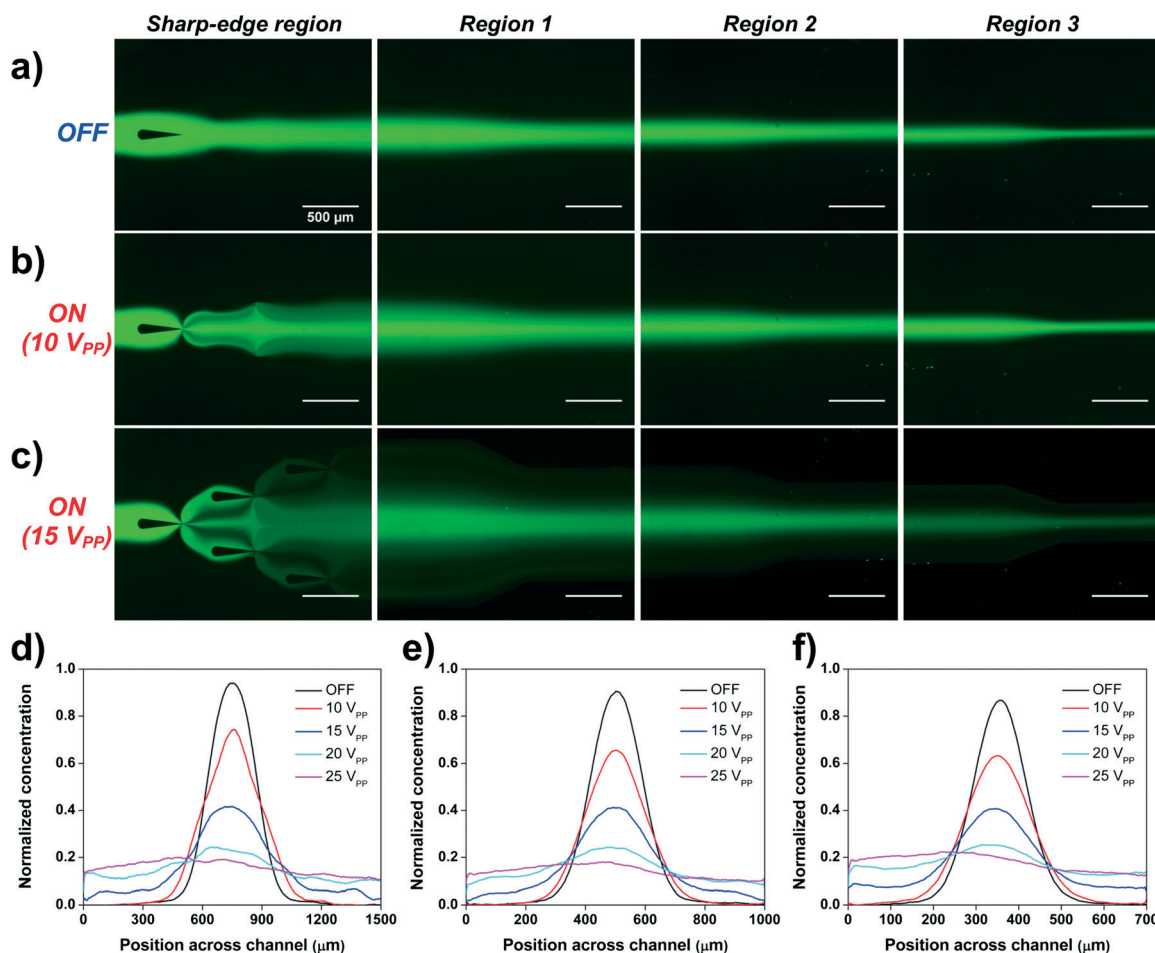


Fig. 3 Fluorescent images of generated FITC-dextran gradients at different regions (from left to right: sharp-edge-structure region, region 1, region 2, and region 3) when (a) the piezoelectric transducer is inactive, and the piezoelectric transducer is on at (b) 10 V_{PP} and (c) 15 V_{PP} . The plots show the corresponding gradient profiles under different voltages at three regions downstream the channel: (d) region 1: 1500 μm wide, (e) region 2: 1000 μm wide, and (f) region 3: 700 μm wide. The results show that spatially controlled gradients may be generated by adjusting the input voltage of the piezoelectric transducer and the channel width downstream the channel.

arrangement of sharp-edge structures, a mono-directional, linear gradient was generated. By adjusting the driving voltage of the piezoelectric transducer, the gradient profile was adjusted accordingly. Additionally, the temporal controllability of this type of gradient was also tested by alternating the piezoelectric transducer (Video S4[†]). The results show the flexibility of our sharp-edge-based gradient generator. In other words, we can, in conjunction with the simulation approach we reported,⁶² arrange the sharp-edge structures differently to establish concentration gradients with prescribed characteristics.

The effect of flow rate on the gradient generation

Our acoustofluidic gradient generator mixes two fluids as induced by the acoustic streaming effect. This effect can be suppressed by introducing higher flow rates into the channel.^{61,62} In this work we also investigated the effect of flow rate, including the total flow rate ($Q_{\text{TOTAL}} = Q_{\text{PBS}} + Q_{\text{FITC}}$) and the flow rate ratio inside the channel, on the formation of a

FITC-dextran concentration gradient under a constant driving voltage. When studying the effect of total flow rate, we kept the flow rate ratio constant ($R_{\text{FLOW}} = 5$), while gradually increasing the flow rates of PBS and FITC-dextran. Fig. 4a shows the fluorescent images captured at the sharp-edge-structure region when various total flow rates were applied with a driving voltage of 25 V_{PP} . At a lower total flow rate ($Q_{\text{TOTAL}} = 3 \mu\text{L min}^{-1}$; $Q_{\text{PBS}} = 2.5 \mu\text{L min}^{-1}$; $Q_{\text{FITC}} = 0.5 \mu\text{L min}^{-1}$), a nearly-complete mixing of FITC and PBS in the channel was observed (Fig. 4a), yielding a flat concentration profile (Fig. 4c). Along with the increase in total flow rate, the mixing width was reduced (Fig. 4a), forming steeper gradient profiles (Fig. 4c). The results suggest that under a fixed input voltage, the ability to oscillate sharp-edge structures to induce acoustic streaming could be suppressed by high flow rates, which is in accordance with our previous finding.^{61,62} In other words, we could alternate the total flow rate to adjust the gradient profiles. Under two different flow rates, mixing behavior at the sharp-edge-structure region was compared in response to the change in driving voltage (Fig. S3[†]).

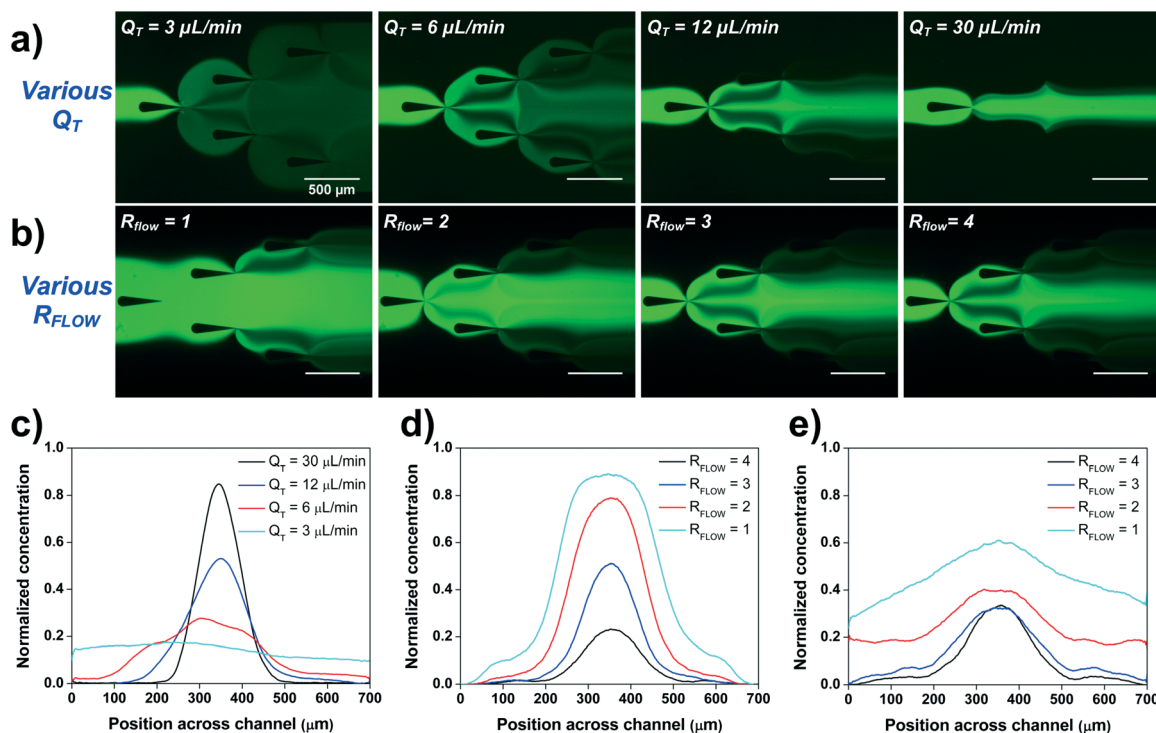


Fig. 4 Fluorescent images of mixing behavior of FITC-dextran and DI water at the sharp-edge-structure region by varying (a) the total flow rates of the fluids inside the channel (the flow ratio remained constant), and (b) the flow rate ratio of the two fluids (the total flow rate remained constant). The plots show the corresponding gradient profiles at region 3 downstream the channel by changing (c) the total flow rates of the fluids inside the channel (the flow ratio remains constant, *i.e.*, $R_{\text{FLOW}} = 5$), (d) the flow rate ratio of the two fluids (the total flow rate remains constant), and (e) the flow rate ratio of the two fluids (the total flow rate is varied). These results demonstrate that by adjusting the total flow rate and the flow rate ratio, various gradient profiles may be generated using our acoustofluidic device.

When changing the flow rate ratio while maintaining the total flow rate ($Q_{\text{TOTAL}} = 6 \mu\text{L min}^{-1}$) and the driving voltage (25 V_{PP}), we could shift the position of the interface of two solutions. As such we established various concentration gradient profiles (Fig. 4b and d). Moreover, as shown in Fig. 4e, once the total flow rate was changed along with the flow rate ratio ($Q_{\text{FITC}} = 1 \mu\text{L min}^{-1} = \text{constant}$), we generated gradient profiles (Fig. 4e) different from those in Fig. 4d. The results once again show that with our device, the widths and heights of gradient profiles (or a related measure such as the slope of a gradient profile) are easily controlled by adjusting the flow rates of two solutions.

Temporal control of gradient generation

In contrast to existing passive gradient generators,^{33,34} our device generates concentration gradients in an active fashion – a feature of particular importance for time-dependent cell studies. Aside from the ability to generate static concentration gradients of various profiles by adjusting the flow rate and the input voltage, our acoustofluidic device generates temporally controllable gradients by modulation of the input signal of the piezoelectric transducer. Fig. 5a shows the fluorescent images of a complete cycle of gradient generation by

alternately triggering the piezoelectric transducer with a period (T_{Trigger}) of 4 seconds (*i.e.*, 2 s ON and 2 s OFF). Alternating the piezoelectric transducer, we generated an alternating gradient profile at an alternating frequency of 0.25 Hz (Video S2† and Fig. 5b), which is comparable to other existing acoustic-based gradient generators.^{39,40} By adjusting the triggering period, we will be able to generate gradient profiles of various alternating frequencies. The results demonstrate that our device generates not only spatial concentration gradients, but also temporal concentration gradients. The temporal resolution of our acoustofluidic gradient generator, namely the alternating frequency, can be further improved by increasing the flow rate, or even changing the arrangement of the sharp-edge structures; however, there are a few things that need to be taken into consideration. Increasing flow rate, for example, may also generate high flow shear stresses that may result in undesirable cellular behavior; additionally, when introducing high flow rates, higher driving voltages would be required to generate gradient profiles similar to those generated under low flow rates.

To further demonstrate the spatiotemporal controllability of our acoustofluidic gradient generator, we alternated the piezoelectric transducer by sweeping the driving frequency for different time intervals. Fig. 5c and d show the corresponding concentration profiles at the region of interest

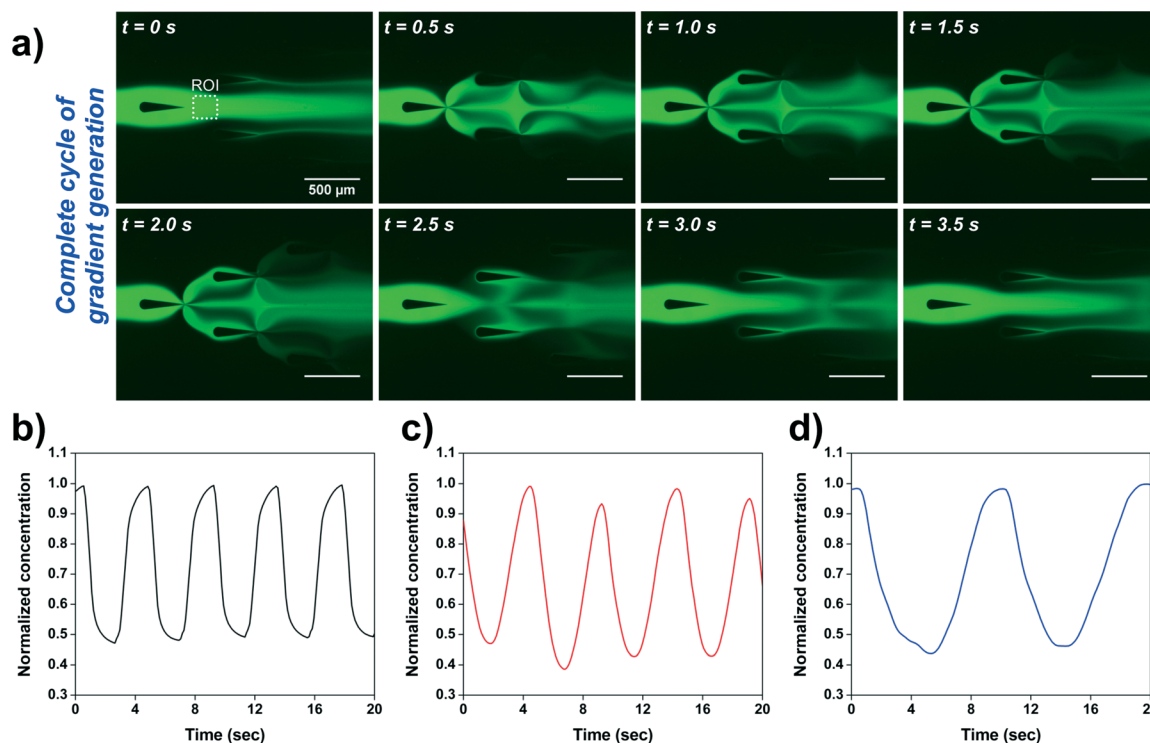


Fig. 5 (a) Fluorescent images showing a complete cycle of gradient generation at an ON/OFF frequency of 0.25 Hz ($T = 4$ s). The plots show the corresponding fluorescence intensity profiles at regions of interest (ROI) in (a), when the gradient generator was operated at (b) an ON/OFF frequency of 0.25 Hz, (c) by sweeping the working frequency of the piezoelectric transducer from 13 kHz to 14 kHz within 4 s, and (d) within 8 s. The results demonstrate the spatiotemporal control of the chemical gradient generation using our acoustofluidic device.

(ROI) by sweeping the driving frequency from 13.0 to 14.0 kHz, respectively, with sweeping times (T_{sweep}) of 4 and 8 seconds (Video S5†). We generated spatiotemporally controllable gradient profiles, and this capability can be useful to elucidate time-resolving cellular signaling dynamics.

Cell migration in our acoustofluidic device

Thus far, we have demonstrated the capability and spatiotemporal controllability of our sharp-edge-based gradient generator *via* the aforementioned experiments and characterizations. To further validate our device for cell studies (*i.e.*,

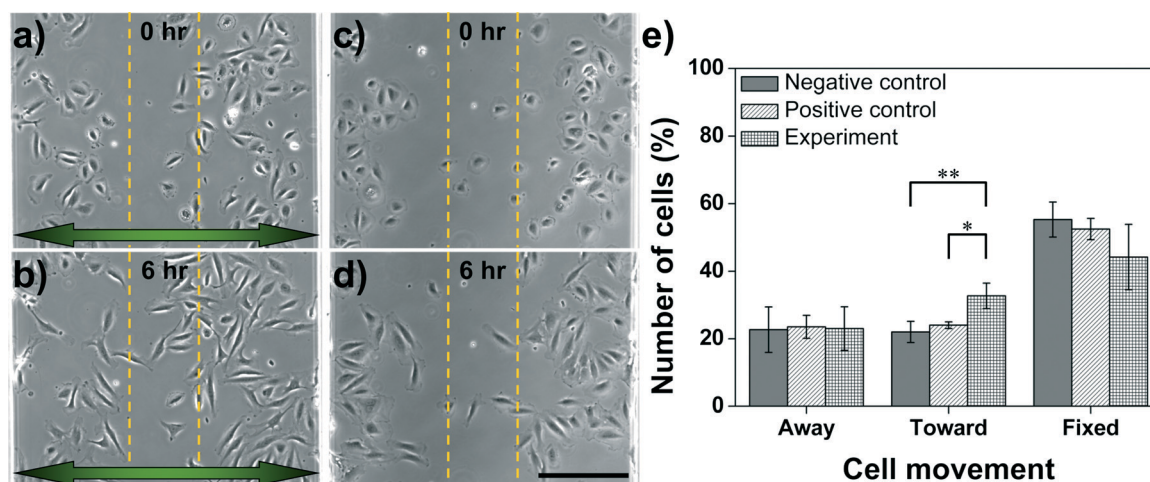


Fig. 6 HMVEC-d chemotaxis in the cell culture chamber. (a, b) Representative phase contrast image of cell positions at time = 0, 6 hours during chemotaxis. (c, d) Representative phase contrast images of cell positions at time = 0, 6 hours when only pure medium was present. The arrow points toward lower VEGF concentrations. (e) The percentage of cell movement in the cell culture chamber under various VEGF concentration conditions. Data represent averages of $n = 3$ independent experiments \pm standard deviation (* $p < 0.05$, ** $p < 0.01$). Scale bar: 200 μm .

applicability and biocompatibility), we conducted HMVEC-d cell migration experiments within our acoustofluidic gradient generator.

To demonstrate HMVEC-d cell migration in response to a VEGF concentration gradient generated by our device, the channels were injected with pure EndoGro-LS media and EndoGro-LS containing VEGF, respectively, at $Q_{\text{EndoGro}} = 2.5 \text{ mL min}^{-1}$ and $Q_{\text{VEGF}} = 0.5 \text{ mL min}^{-1}$. Under an input voltage of $15 V_{\text{PP}}$, a VEGF gradient profile as shown in Fig. 3f ($15 V_{\text{PP}}$) was generated with a maximum concentration of $\sim 25 \text{ ng mL}^{-1}$ in the center of the channel, and a minimum concentration of $\sim 10 \text{ ng mL}^{-1}$ near both the sidewalls. The position of each HMVEC-d cell was recorded by taking images every 5 minutes, from $t = 0$ to 6 hours. Fig. 6a and b show the relative position of HMVEC-d cells, respectively, before and after 6 hours' exposure to the VEGF gradient (experimental group). As shown in Fig. 6e, when exposed to the VEGF gradient for 6 hours, 33% of the cells seeded initially in the two sidewall zones had migrated toward the center of the channel (higher VEGF concentration), 23% of the cells migrated toward the sidewall (lower VEGF concentration), and 44% barely moved. In the absence of a VEGF gradient (negative-control group: pure medium only), by contrast, a striking decrease of nearly 11% (from 33% to 22%) in the number of cells migrating toward the center was observed, along with changes in the number of cells moving toward the sidewall (23%) and barely moving (55%). Additionally, in the presence of a VEGF gradient which was formed solely from diffusion (positive control group; Fig. 3f), the number of cells moving toward the center increased by only about 2% (from 22% to 24%), with insignificant changes in the number of cells moving toward the

sidewall ($\sim 24\%$) and barely moving ($\sim 52\%$). Collectively, the number of cells moving toward the center when exposed to a VEGF gradient was statistically greater than those which were exposed to the pure medium and the diffusion-based VEGF gradient. The results demonstrate that our acoustofluidic device generates VEGF gradients which in turn initiate HMVEC-d chemotaxis, demonstrating the capability of our device for cell chemotaxis studies. Time-lapse images showing the HMVEC-d migration inside the channel of our device over 6 hours and 16 hours can be found in ESI† (Video S6).

Cell viability in the presence of lasting acoustic field

Our acoustofluidic device operates based upon acoustic streaming effects induced by the activation of a piezoelectric transducer. We assessed cell viability upon acoustic streaming induced by sharp-edge structures as well as an applied acoustic field, by subjecting cells to the acoustic field for 6 hours (driving voltage = $20 V_{\text{PP}}$). Fig. 7 illustrates cell viability within the channel of our gradient generation device. As the representative bright-field images show, we monitored the cell viability for cells which were seeded in the sharp-edge-structure region and the migration region (region 3) (Fig. 7a). After 6 hours' exposure to the acoustic field, HMVEC-d cells still adhered to the substrate without any irregular morphology. Further, the HMVEC-d cells seeded in both the sharp-edge-structure region and the migration region remained viable; no dead cells were observed (Fig. 7b). The results are comparable to those obtained in control-group experiments (absence of an acoustic field) (Fig. 7c). These results illustrate

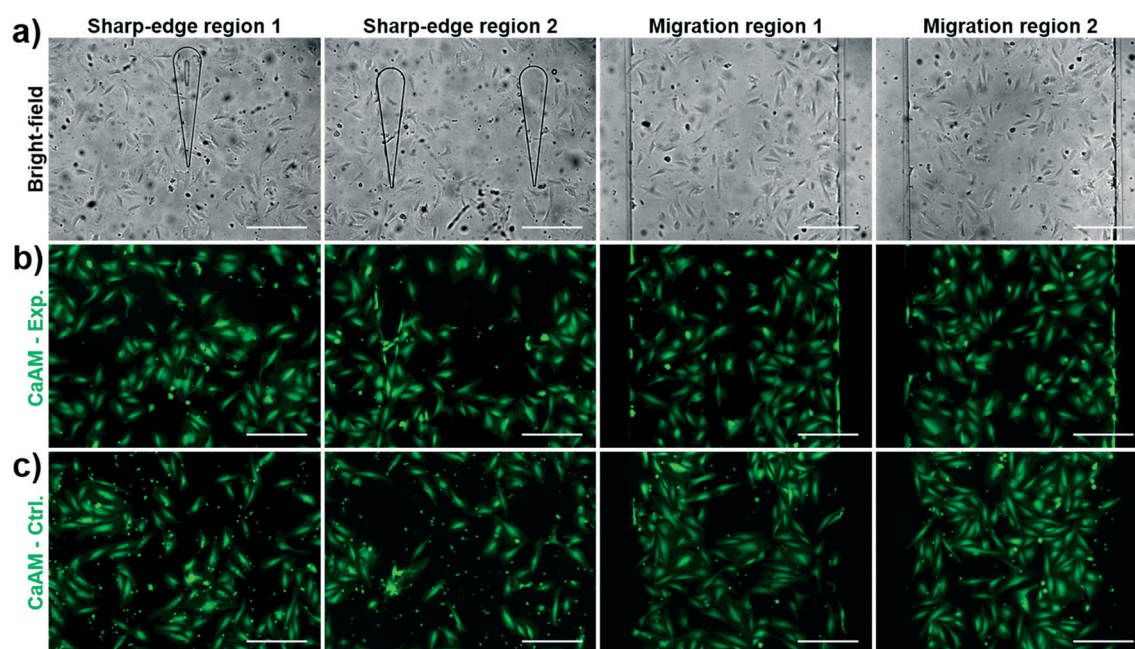


Fig. 7 (a) Representative bright field (BF) images showing the cell morphology at sharp-edge-structure regions and cell migration regions. Corresponding fluorescent images showing the cell viability after 6 hours (b) in the absence of an acoustic field (control group) and (c) in the presence of an acoustic field (experimental group). Scale bar: $200 \mu\text{m}$.

that our acoustofluidic gradient-generation device is biocompatible.

Extending the assessment of cell viability, we found that after 16 hours' exposure to an acoustic field (driving voltage = 20 V_{pp}), the HMVEC-d cells were still viable and present with normal morphology at different regions inside the channel (Fig. S4†). These results again prove our device biocompatible, as well as viable for cell studies where long-term cell culture is required.

Conclusions

Chemical gradient which are spatiotemporally stable and of tunable concentration can be generated using our sharp-edge-based acoustofluidic gradient generator. In contrast to existing microfluidic gradient generators, in which the gradients are formed solely based on passive mechanisms, our device forms gradients in an active, controllable manner. Using our device, it is possible to generate gradients with complex profiles by changing the flow rate ratio of co-flowing fluids (stimulant and buffer), the driving voltage of the piezoelectric transducer, and the arrangement of sharp-edge structures (spacing). Moreover, temporally changing gradients can be easily generated by varying the driving voltage and the actuation time of the piezoelectric transducer. Our device is well-suited for many chemical/biological studies and applications, such as investigating cell chemotaxis, differentiation, migration, and drug discovery in dynamic chemical environments. The effect of pulsatile chemical gradient upon cellular dynamics can be unveiled and much temporal information about cell signaling will be extracted upon development of our platform.

Acknowledgements

This research was supported by National Institutes of Health (1 R01 GM112048-01A1 and 1R33EB019785-01), National Science Foundation (CBET-1438126 and IIP-1534645), and the Penn State Center for Nanoscale Science (MRSEC) under grant DMR-1420620. Components of this work were conducted at the Penn State node of the NSF-funded National Nanotechnology Infrastructure Network.

References

- 1 E. K. Sackmann, A. L. Fulton and D. J. Beebe, *Nature*, 2014, **507**, 181–189.
- 2 E. Berthier and D. J. Beebe, *Lab Chip*, 2014, **12**, 3241–3247.
- 3 S. Kim, H. J. Kim and N. L. Jeon, *Integr. Biol.*, 2010, **2**, 584–603.
- 4 T. M. Keenan and A. Folch, *Lab Chip*, 2008, **8**, 34–57.
- 5 C. Y. Chan, P.-H. Huang, F. Guo, X. Ding, V. Kapur, J. D. Mai, P. K. Yuen and T. J. Huang, *Lab Chip*, 2013, **13**, 4697–4710.
- 6 D. Irimia, *Annu. Rev. Biomed. Eng.*, 2010, **12**, 259–284.
- 7 A. Ainla, E. T. Jansson, N. Stepanyants, O. Orwar and A. Jesorka, *Anal. Chem.*, 2010, **82**, 4529–4536.
- 8 J. Atencia, G. A. Cooksey and L. E. Locascio, *Lab Chip*, 2012, **12**, 309–316.
- 9 J. van Zon, M. Barkoulas and A. van Oudenaarden, *Nat. Commun.*, 2014, **6**, 1–11.
- 10 D. Jowhar, G. Wright, P. C. Samson, J. P. Wikswo and C. Janetopoulos, *Integr. Biol.*, 2010, **2**, 648–658.
- 11 T. S. Shimizu, Y. Tu and H. C. Berg, *Mol. Syst. Biol.*, 2010, **6**, 382.
- 12 T. Ahmed, T. S. Shimizu and R. Stocker, *Nano Lett.*, 2010, **10**, 3379–3385.
- 13 N. L. Jeon, H. Baskaran, S. K. W. Dertinger, G. M. Whitesides, L. van de Water and M. Toner, *Nat. Biotechnol.*, 2002, **20**, 826–830.
- 14 A. Nakajima, S. Ishihara, D. Imoto and S. Sawai, *Nat. Commun.*, 2014, **5**, 1–14.
- 15 B. Meier, A. Zielinski, C. Weber, D. Arcizet, S. Youssef, T. Franosch, J. O. Rädler and D. Heinrich, *Proc. Natl. Acad. Sci. U. S. A.*, 2011, **108**, 11417–11422.
- 16 B. G. Chung, L. A. Flanagan, S. W. Rhee, P. H. Schwartz, A. P. Lee, E. S. Monuki and N. L. Jeon, *Lab Chip*, 2005, **5**, 401–406.
- 17 A. Shamloo, M. Heibatollahi and M. R. K. Mofrad, *Integr. Biol.*, 2015, **7**, 335–344.
- 18 J. Y. Park, C. M. Hwang, S. H. Lee and S.-H. Lee, *Lab Chip*, 2007, **7**, 1673–1680.
- 19 S. J. Wang, W. Saadi, F. Lin, C. Minh-Canh Nguyen and N. L. Jeon, *Exp. Cell Res.*, 2004, **300**, 180–189.
- 20 B. Lin, T. Yin, Y. I. Wu, T. Inoue and A. Levchenko, *Nat. Commun.*, 2015, **6**, 6619.
- 21 S. Boyden, *J. Exp. Med.*, 1962, **115**, 453–466.
- 22 S. H. Zigmond, *J. Cell Biol.*, 1977, **75**, 606–616.
- 23 D. Zicha, G. A. Dunn and A. F. Brown, *J. Cell Sci.*, 1991, **99**(Pt 4), 769–775.
- 24 R. W. Gundersen and J. N. Barrett, *Science*, 1979, **206**, 1079–1080.
- 25 H. Song, G. Ming, Z. He, M. Lehmann, L. McKerracher, M. Tessier-Lavigne and M. Poo, *Science*, 1998, **281**, 1515–1518.
- 26 F. Lin, W. Saadi, S. W. Rhee, S.-J. Wang, S. Mittal and N. L. Jeon, *Lab Chip*, 2004, **4**, 164–167.
- 27 D. Irimia, S.-Y. Liu, W. G. Tharp, A. Samadani, M. Toner and M. C. Poznansky, *Lab Chip*, 2006, **6**, 191–198.
- 28 T. M. Keenan, C. H. Hsu and A. Folch, *Appl. Phys. Lett.*, 2006, **89**, 114103.
- 29 B. G. Chung, F. Lin and N. L. Jeon, *Lab Chip*, 2006, **6**, 764–768.
- 30 B. Mosadegh, C. Huango, J. W. Park, H. S. Shin, B. G. Chung, S. K. Hwang, K. H. Lee, H. J. Kim, J. Brody and N. L. Jeon, *Langmuir*, 2007, **23**, 10910–10912.
- 31 W. Saadi, S. W. Rhee, F. Lin, B. Vahidi, B. G. Chung and N. L. Jeon, *Biomed. Microdevices*, 2007, **9**, 627–635.
- 32 A. Shamloo, N. Ma, M.-M. Poo, L. L. Sohn and S. C. Heilshorn, *Lab Chip*, 2008, **8**, 1292–1299.
- 33 S. K. W. Dertinger, D. T. Chiu, N. L. Jeon and G. M. Whitesides, *Anal. Chem.*, 2001, **73**, 1240–1246.
- 34 N. L. Jeon, S. K. W. Dertinger, D. T. Chiu, I. S. Choi, A. D. Stroock and G. M. Whitesides, *Langmuir*, 2000, **16**, 8311–8316.

- 35 H. Wu, B. Huang and R. N. Zare, *J. Am. Chem. Soc.*, 2006, **128**, 4194–4195.
- 36 J. Atencia, J. Morrow and L. E. Locascio, *Lab Chip*, 2009, **9**, 2707–2714.
- 37 K. Hattori, S. Sugiura and T. Kanamori, *Lab Chip*, 2009, **9**, 1763–1772.
- 38 T. Frank and S. Tay, *Lab Chip*, 2013, **13**, 1273–1281.
- 39 G. Destgeer, S. Im, B. H. Ha, J. H. Jung, M. A. Ansari and H. Jin Sung, *Appl. Phys. Lett.*, 2014, **104**, 023056.
- 40 D. Ahmed, C. Y. Chan, S.-C. S. Lin, H. S. Muddana, N. Nama, S. J. Benkovic and T. J. Huang, *Lab Chip*, 2013, **13**, 328–331.
- 41 P.-H. Huang, M. I. Lapsley, D. Ahmed, Y. Chen, L. Wang and T. J. Huang, *Appl. Phys. Lett.*, 2012, **101**, 141101.
- 42 A. R. Tovar, M. V. Patel and A. P. Lee, *Microfluid. Nanofluid.*, 2011, **10**, 1269–1278.
- 43 D. Ahmed, X. Mao, B. K. Juluri and T. J. Huang, *Microfluid. Nanofluid.*, 2009, **7**, 727–731.
- 44 D. Ahmed, X. Mao, J. Shi, B. K. Juluri and T. J. Huang, *Lab Chip*, 2009, **9**, 2738–2741.
- 45 H. Bruus, *Lab Chip*, 2012, **12**, 20–28.
- 46 M. Wiklund, R. Green and M. Ohlin, *Lab Chip*, 2012, **12**, 2438–2451.
- 47 P. Li, Z. Mao, Z. Peng, L. Zhou, Y. Chen, P.-H. Huang, C. I. Truica, J. J. Drabick, W. S. El-Deiry, M. Dao, S. Suresh and T. J. Huang, *Proc. Natl. Acad. Sci. U. S. A.*, 2015, **112**, 4970–4975.
- 48 P. B. Muller, R. Barnkob, M. J. H. Jensen and H. Bruus, *Lab Chip*, 2012, **12**, 4617–4627.
- 49 Y. Chen, A. A. Nawaz, Y. Zhao, P.-H. Huang, J. P. McCoy, S. J. Levine, L. Wang and T. J. Huang, *Lab Chip*, 2014, **14**, 916–923.
- 50 Y. Xu, A. Hashmi, G. Yu, X. Lu, H.-J. Kwon, X. Chen and J. Xu, *Appl. Phys. Lett.*, 2013, **102**, 023702.
- 51 A. Hashmi, G. Heiman, G. Yu, M. Lewis, H. J. Kwon and J. Xu, *Microfluid. Nanofluid.*, 2013, **14**, 591–596.
- 52 W.-K. Tseng, J.-L. Lin, W.-C. Sung, S.-H. Chen and G.-B. Lee, *J. Micromech. Microeng.*, 2006, **16**, 539–548.
- 53 I. Iranmanesh, R. Barnkob, H. Bruus and M. Wiklund, *J. Micromech. Microeng.*, 2013, **23**, 105002.
- 54 Y. Chen, X. Ding, S.-C. Steven Lin, S. Yang, P.-H. Huang, N. Nama, Y. Zhao, A. A. Nawaz, F. Guo, W. Wang, Y. Gu, T. E. Mallouk and T. J. Huang, *ACS Nano*, 2013, **7**, 3306–3314.
- 55 F. Guo, P. Li, J. B. French, Z. Mao, H. Zhao, S. Li, N. Nama and J. R. Fick, *Proc. Natl. Acad. Sci. U. S. A.*, 2015, **112**, 43–48.
- 56 J. Shi, D. Ahmed, X. Mao, S.-C. S. Lin, A. Lawit and T. J. Huang, *Lab Chip*, 2009, **9**, 2890–2895.
- 57 J. Shi, H. Huang, Z. Stratton, Y. Huang and T. J. Huang, *Lab Chip*, 2009, **9**, 3354–3359.
- 58 X. Ding, S.-C. S. Lin, B. Kiraly, H. Yue, S. Li, I.-K. Chiang, J. Shi, S. J. Benkovic and T. J. Huang, *Proc. Natl. Acad. Sci. U. S. A.*, 2012, **109**, 11105–11109.
- 59 S. Li, X. Ding, F. Guo, Y. Chen, M. I. Lapsley, S.-C. S. Lin, L. Wang, J. P. McCoy, C. E. Cameron and T. J. Huang, *Anal. Chem.*, 2013, **85**, 5468–5474.
- 60 X. Ding, Z. Peng, S.-C. S. Lin, M. Geri, S. Li, P. Li, Y. Chen, M. Dao, S. Suresh and T. J. Huang, *Proc. Natl. Acad. Sci. U. S. A.*, 2014, **111**, 12992–12997.
- 61 P.-H. Huang, Y. Xie, D. Ahmed, J. Rufo, N. Nama, Y. Chen, C. Y. Chan and T. J. Huang, *Lab Chip*, 2013, **13**, 3847–3852.
- 62 N. Nama, P.-H. Huang, T. J. Huang and F. Costanzo, *Lab Chip*, 2014, **14**, 2824–2836.
- 63 P.-H. Huang, N. Nama, Z. Mao, P. Li, J. Rufo, Y. Chen, Y. Xie, C.-H. Wei, L. Wang and T. J. Huang, *Lab Chip*, 2014, **14**, 4319–4323.
- 64 P.-H. Huang, L. Ren, N. Nama, S. Li, P. Li, X. Yao, R. A. Cuento, C.-H. Wei, Y. Chen, Y. Xie, A. A. Nawaz, Y. G. Alevy, M. J. Holtzman, J. P. McCoy, S. J. Levine and T. J. Huang, *Lab Chip*, 2015, **15**, 3125–3131.
- 65 X. Ding, P. Li, S.-C. S. Lin, Z. S. Stratton, N. Nama, F. Guo, D. Slotcavage, X. Mao, J. Shi, F. Costanzo and T. J. Huang, *Lab Chip*, 2013, **13**, 3626–3649.